IEEE Access
Multidisciplinary | Rapid Review | Open Access Journal

Received September 29, 2021, accepted December 15, 2021, date of publication December 23, 2021,
date of current version January 5, 2022.

Digital Object Identifier 10.1109/ACCESS.2021.3137880

Fractional-Slot PMSMs With One Coil Parallel Branches Made Phases–Part 2: Circulating Harmonic Current Rejection Potential

AHMED MASMOUDI[1], (Senior Member, IEEE), SAHAR MKAOUAR[1], AICHA MAAOUI[1], AND MICHAEL SCHIER[2], (Member, IEEE)
[1]Laboratory of Renewable Energies and Electric Vehicles (RELEV), Sfax Engineering National School, University of Sfax, Sfax 3038, Tunisia
[2]Institute of Vehicle Concepts, German Aerospace Center, 70569 Stuttgart, Germany

Corresponding author: Ahmed Masmoudi (a.masmoudi@enis.rnu.tn)

This work was supported in part by the European Union through the Erasmus Exchange Program 20210607-ENIS-KA107 that enabled the mobility of Sahar Mkaouar to the University of Kassel, Germany, and in part by the Tunisian Ministry of Higher Education and Scientific Research in the framework of the project RELEV-LR13ES24 that partly covered the expenses of the trainee carried out by Aicha Maaoui at the German Aerospace Center. This work represents a synthesis of the Sustainable Mobility Actuators: Research and Technology–(SMART) master projects of Sahar and Aicha.

ABSTRACT The paper is aimed at a class of fractional-slot permanent magnet- synchronous machines (FSPMSMs) equipped with phases made up of one coil parallel branches, with emphasis on their potential to reject the circulating harmonic currents. Following the identification and topological characterization of this class of machines treated in Part 1, the star of slots approach is extended to the investigation of their back-EMF harmonic content, and the possible resulting circulating harmonic currents. It is found that all identified candidates exhibit the potential to reject the circulating harmonic currents. A case study dedicated to a candidate equipped with three phases made up of six parallel branches of one coil each, is treated. Following an analysis of its back-EMF harmonic content, the torque-speed characteristic is analytically-predicted and validated by 2D finite element analysis and by experiments. The study is achieved by a special attention paid to the iron loss and thermal analysis.

INDEX TERMS Fractional-slot PM synchronous machines, one coil parallel branches made phases, start of slots approach, back-EMF harmonic content, circulating harmonic currents, torque production, power flow and thermal analysis.

I. INTRODUCTION

In recent years, there is an increasing attention to develop fault-tolerant electric drives especially in transportation applications. The emergence of the ''More Electric Aircraft'' trend makes it necessary the development of new electric drives with emphasis on their fault-tolerance capabilities in presence of extreme emergency situations [1]–[3]. Enhanced fault-tolerance capability represents the most vital requirement in aerospace applications in so far as the safety of the passengers is intimately linked.

Fault-tolerant electric drives are also highly coveted in sustainable propulsion systems equipping electric and hybrid vehicles (EVs and HEVs) [4]–[6]. Beyond the zero green house gas emissions, the high efficiency, the possibility to recover the wheel kinetic energy during regenerative braking, the fault tolerance enhances the superiority of the electric and hybrid vehicles over their internal combustion engine propelled counterparts.

A synthesis of a literature review revealed that the fault-tolerant-oriented design of electric machines is dominated by multiphase candidates. The latter are commonly equipped with phases made up of series-connected coils. Nevertheless, such an arrangement compromises their faut-tolerance with respect to open-circuit faults. Moreover, multiphase machines equipped with phases made up of series-connected coils require non conventional inverters with a relatively high DC-bus voltage for their power supply. This results in bulky battery packs in the case of electric and hybrid propulsion systems. Reduced DC-bus voltage drives represent attractive concepts for electric propulsion systems, particularly with the current trend aimed at the integration of the 48V technology

The associate editor coordinating the review of this manuscript and approving it for publication was Shaopeng Wu.

in automotive applications. Among the 48V automotive applications, one can distinguish the mild hybrid propulsion system which has been introduced in early 2000 [7] and manufactured by Audi in 2016.

Recently, *Fatemi et al.* proposed an approach to optimise the design optimization of an electric machine for a 48V mild hybrid vehicle with rotor technology and the slot-pole combinations [8]. To do so, they considered a comparison study of three candidates: (i) a PM synchronous machine (PMSM) with V-shaped rare-earth magnets in the rotor, a PMSM with deep V-shaped ferrite rotor magnets, and a synchronous reluctance machine with four layers of conforming flux barriers. Predictive current control strategies dedicated to a 48V 600W brushless DC motor have been assessed and implemented in [9]. This has been carried in an attempt to accurately track the ideal hexagonal trajectory described by the armature current phasor in the stationary plane.

48V automotive actuators could be suitably-equipped with low-voltage FSPMSMs where the phases are arranged by connecting in parallel branches incorporating a single or several coils. In light of this, a significant improvement in the fault-tolerance capability is gained, such that under an open-circuit fault, the machine would lose the torque produced by the faulty branch, rather than the one developed by a total phase in series-connected coils machines. Furthermore, thanks to their reduced DC bus voltage, EVs and HEVs would have the merit to definitely discard the risk of electrocution of their passengers in case of accidents.

FSPMSMs equipped with odd number of phases, arranged in parallel branches incorporating one coil or suitable combinations of coils, have been partly treated in [10]. A special attention has been paid to assess their torque production capability under open-circuit faulty conditions. Following the identification of the slot/pole combinations enabling the above-described arrangement, two case studies of a 12-slot/10-pole 3 phase and a 20-slot/16-pole 5 phase FSPMSMs have been treated. Their healthy and open-circuit faulty operations have been investigated by 2D FEA.

A comprehensive survey dedicated to a systematic identification and topological characterisation of all FSPMSMs equipped with phases made up of single coil parallel branches, has been proposed in [11]. The targeted topologies exhibit the highest open-circuit fault-tolerance potential on one hand and require the lowest DC-bus voltage on the other hand. A star of slots-based approach enabled the identification of the slot-pole combinations fulfilling the targeted FSPMSMs as well as their winding factors. This has been achieved considering the cases of odd and even number of phases, arranged in single- and double-layer slots.

The present paper takes back the candidates identified in [11], in order to investigate the possible circulating harmonic currents in the loops created by the parallel branches. These would be harmful for the features of the targeted topologies. The investigation is based on an extension of the star of slots approach that enables the prediction of the back-EMF harmonic content. The possible circulating harmonic currents would result from phase shifts between the harmonic back-EMFs induced in the parallel branches. In absence of shifts, harmonic current exist in the parallel branches but not in a circulating form, with their sum flowing in the machine lines.

II. INVESTIGATION OF POSSIBLE CIRCULATING HARMONIC CURRENTS

A. STUDY BACKGROUND

From a fundamental point of view, by connecting in parallel magnetically-coupled circuits, the first issue, that comes in mind, is the possible circulation of harmonic currents in the loops resulting from the parallel connections of these circuits. Such a problem concerns the FSPMSM candidates identified in [11]. Indeed, these have been selected on the basis that all harmonic back-EMFs of rank p (fundamental) induced in the coils assigned to each phase are identical in magnitude and have similar or opposite phases.

With this said, the question that arises immediately is: How about the harmonic back-EMFs of rank n, with $n \neq p$? Any phase shift between the harmonic back-EMFs would result in the circulation of harmonic currents that make the one coil parallel branches arrangement of the phases totally useless. Indeed, the circulating harmonic currents in the loops resulting from the one coil parallel branches would affect the machine torque production and power efficiency. This section puts light on this possible drawback.

B. HARMONIC BACK-EMFs CHARACTERIZATION

Referring to [14], the *Fourrier* expansion of the no-load air gap flux density (produced by the PMs), assuming a slotless machine, could be expressed as:

$$B_{PM}(\theta) = \sum_{n=0,1,2..}^{\infty} B_{(2n+1)} \cos(2n+1)p\theta \qquad (1)$$

where θ is a mechanical angle counted in the air gap starting from the magnetic axis of a north pole magnet. Therefore, only harmonics of odd ranks should be considered in the investigation aimed to the possible circulating harmonic currents.

The investigation of the back-EMF harmonic content goes through the application of the star of slots approach considering an angular shift $\alpha_{(2n+1)}$ between two successive phasors, expressed as [16], [25]:

$$\alpha_{(2n+1)} = (2n+1)p\frac{2\pi}{N_s} \quad with\ n \neq 0 \qquad (2)$$

Then, the back-EMF phasors assigned to each phase, that have been identified by the star of slots corresponding to the fundamental, are reconsidered. In case the harmonic back-EMF phasors induced in all parallel branches of a phase would have the same initial angular shift, this would lead to a circulation of identical harmonic currents in the phase parallel branches. This statement would be true if the line harmonic current of the star-connected machine, is equal to the one of a branch multiplied by the number of parallel branches

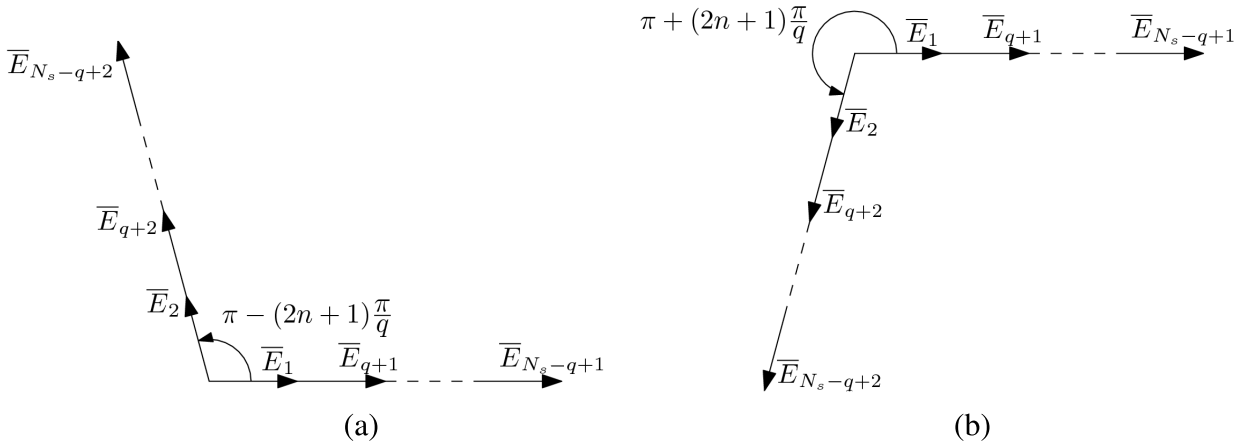

FIGURE 1. Star of slots of the harmonic back-EMF of rank $(2n+1)$ of the FSPMSMs with odd number of phases arranged in double-layer slots in the case where all fundamental back-EMF phasors are aligned in one sector. Legend: (a) two successive harmonic back-EMF phasors shifted by $\pi-(2n+1)\frac{\pi}{q}$, (b) two successive harmonic back-EMF phasors shifted by $\pi+(2n+1)\frac{\pi}{q}$.

per phase. This confirms the absence of circulating harmonic currents in the loops created by the parallel connection of the phase coils.

In what follows, the FSPMSM topologies, enabling the one coil parallel branches made phases, identified in [11], are systematically re-investigated with emphasis on their back-EMF harmonic content.

C. CASE OF ODD NUMBER OF PHASES

1) CASE OF DOUBLE-LAYER SLOTS

The star of slots of the back-EMF harmonic of rank $(2n+1)$ with $n \neq 0$ of the FSPMSMs identified in paragraph II-A1 (case 1) of Part 1 [11], are shown in Fig. 1. In the case where two successive harmonic back-EMF phasors are shifted by $\left(\frac{q-1}{q}\right)\pi$, the corresponding harmonic back-EMF phasors of rank $(2n+1)$ are shifted by $\pi-(2n+1)\frac{\pi}{q}$. In the case where two successive fundamental back-EMF phasors are shifted by $\left(\frac{q+1}{q}\right)\pi$, the corresponding harmonic back-EMF phasors of rank $(2n+1)$ are shifted by $\pi+(2n+1)\frac{\pi}{q}$.

In the manner of the fundamental back-EMF, one can notice that the phasors of all harmonic back-EMFs induced in the coils assigned to the phases given in Fig. 1 of Part 1 are aligned, having the same magnitude and initial phase. This results in null circulating harmonic currents in the loops created by the parallel connections of the coils. Referring to the star of slots of Fig. 1, the winding factor of the back-EMF harmonic of rank $(2n+1)$ could be expressed as follows:

$$K^{dl}_{w(2n+1)} = \left|\cos\left((2n+1)\frac{\pi}{2q}\right)\right| \tag{3}$$

Concerning the topologies fulfilling the star of slots treated in paragraph II-A1 (case 2) of Part 1 [11], the corresponding back-EMF harmonics are characterized by the star of slots shown in Fig. 2. The analysis of this latter reveals that all phasors of the back-EMF harmonics induced in the the parallel branches of a phase are identical (having the same magnitude and initial phase). Consequently, one can clearly confirm that no circulating harmonic currents exist in the loops created by the parallel connection of the coils. The winding factor of the harmonic back-EMF of rank $(2n+1)$ is deduced from Fig. 2, as:

$$K^{dl}_{w(2n+1)} = \left|\sin\left((2n+1)\frac{\pi}{2q}\right)\right| \tag{4}$$

2) CASE OF SINGLE-LAYER SLOTS

Following the removal of the phasors of even number from the star of slots illustrated in Figs. 1 and 2, the back-EMF harmonics induced in the one coil parallel branches of the considered phase remain similar, resulting in null circulating harmonic currents. The corresponding expressions of the winding factor $K^{sl}_{w(2n+1)}$ are then the same as the ones of $K^{dl}_{w(2n+1)}$ given by expression (3) and (4), respectively.

The star of slots of the harmonic back-EMF of rank $(2n+1)$ with $n \neq 0$ of the FSPMSMs identified in paragraph II-A2 (second approach) of Part 1, are shown in Fig. 3. One can notice that the harmonic back-EMF phasors of a given phase are identical, resulting in null circulating harmonic currents. The winding factor $K^{sl}_{w(2n+1)}$ is expressed as:

$$K^{sl}_{w(2n+1)} = \left|\cos\left((2n+1)\frac{\pi}{4q}\right)\right| \tag{5}$$

D. CASE OF EVEN NUMBER OF PHASES

1) CASE OF DOUBLE-LAYER SLOTS

The star of slots of the harmonic back-EMF of rank $(2n+1)p$ with $n \neq 0$ of the FSPMSMs identified in paragraph II-B1 of Part 1 [11], are illustrated in Fig. 4. It reveals the absence of circulating harmonic currents.

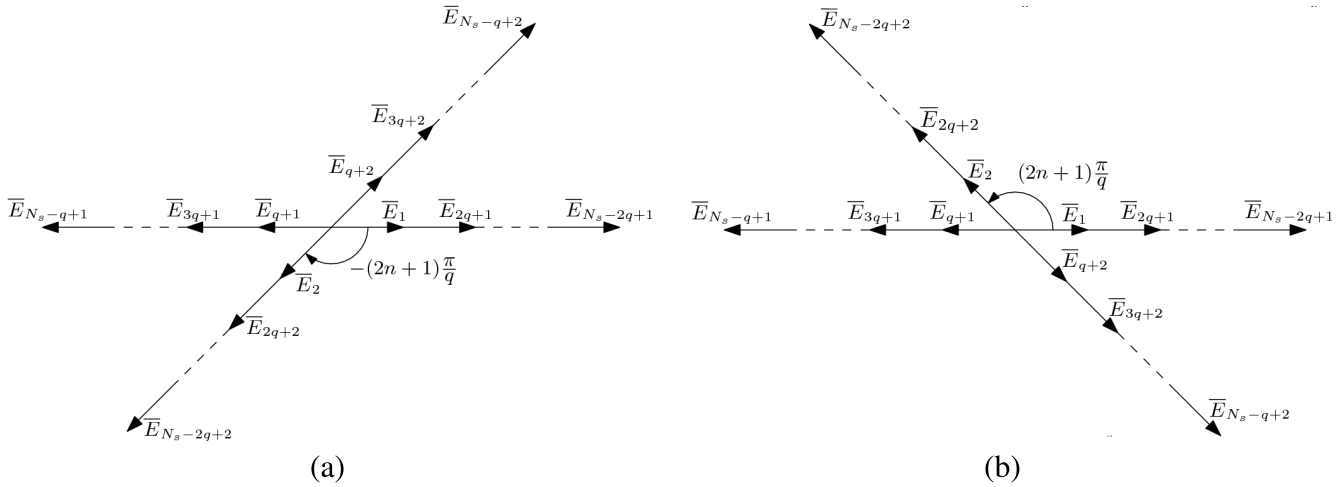

FIGURE 2. Star of slots of the back-EMF harmonic of rank $(2n+1)$ of FSPMSMs with odd number of phases arranged in double-layer slots in the case where half of the fundamental back-EMF phasors are aligned in one sector and the remaining ones are aligned in the opposite sector. Legend: (a) two successive back-EMFs shifted by $-(2n+1)\frac{\pi}{q}$, (b) two successive back-EMFs shifted by $(2n+1)\frac{\pi}{q}$.

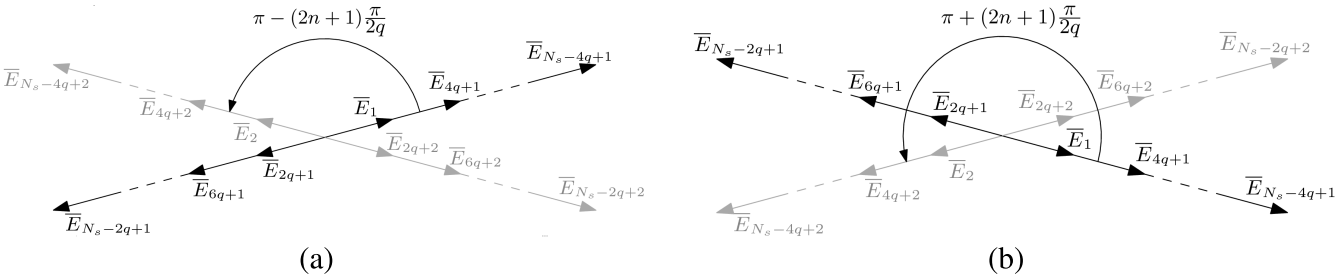

FIGURE 3. Star of slots of the back-EMF harmonic of rank $(2n+1)$ of FSPMSMs with odd number of phases arranged in single-layer slots. **Legend: (black): back-EMFs phasors of the coils inserted in single-layer slots, (gray) back-EMFs phasors removed in the case of single-layer slots.**

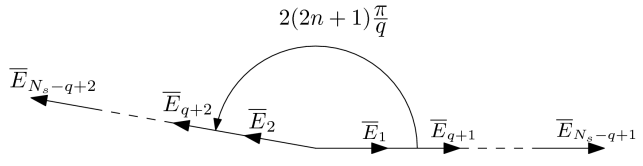

FIGURE 4. Star of slots of the harmonic back-EMF of rank $(2n+1)$ of FSPMSMs with even number of phases arranged in double-layer slots.

Based on Fig. 4, the prediction of the winding factor $K^{dl}_{w(2n+1)}$ of the back-EMF harmonic of rank $(2n+1)$ yields:

$$K^{dl}_{w(2n+1)} = \left|\sin\left((2n+1)\frac{\pi}{q}\right)\right| \tag{6}$$

2) CASE OF SINGLE-LAYER SLOTS

Following the removal of the phasors of even number from the star of slots shown in Fig. 4, the similitude of the harmonic back-EMFs induced in the one coil parallel branches of the considered phase, remains fulfilled, resulting in null circulating harmonic currents. The expression of the winding factor $K^{sl}_{w(2n+1)p}$ is then the same as $K^{dl}_{w(2n+1)p}$ given in (6).

Moreover, Fig. 5 represents the star of slots of the harmonic back-EMF of rank $(2n+1)$ with $n \neq 0$ of the FSPMSMs identified in paragraph II-B2 of Part 1 [11]. Referring to Fig. 5, the prediction of the winding factor of the harmonic back-EMF $K^{dl}_{w(2n+1)}$ of rank $(2n+1)$ has led to the following:

$$K^{sl}_{w(2n+1)} = \left|\cos\left((2n+1)\frac{\pi}{2q}\right)\right| \tag{7}$$

E. SUMMARY

To sum up, it has been found that:

- all FSPMSMs equipped with phases made up of one coil parallel branches, identified in Part 1 [11], have the faculty to reject the circulating harmonic currents. With this said, two cases could be distinguished:
  1) the harmonic winding factor is null. Consequently, the corresponding back-EMF harmonic is discarded, resulting in a null harmonic current in the phase parallel branches,
  2) the harmonic winding factor is not null. This results in a circulation of harmonic currents in the phase branches but not in a circulating form in the loops created by the parallel connection of these branches.

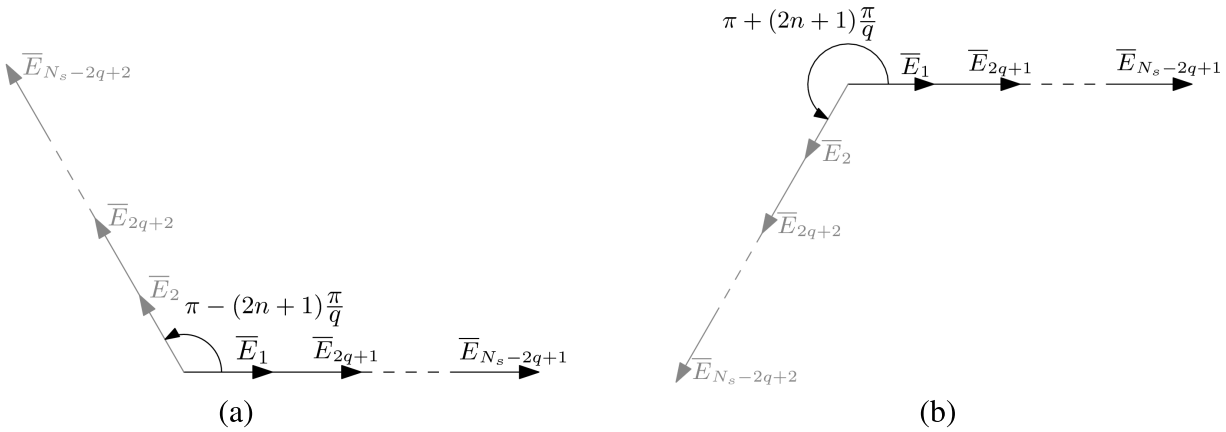

FIGURE 5. Star of slots of the harmonic back-EMF of rank $(2n+1)$ of FSPMSMs with even number of phases arranged in single-layer slots. Legend: (a) two successive harmonic back-EMF phasors shifted by $\pi-(2n+1)\frac{\pi}{q}$, (b) two successive harmonic back-EMF phasors shifted by $\pi+(2n+1)\frac{\pi}{q}$.

- in the manner of the fundamental back-EMFs, in both cases of odd and even number of phases and for a given harmonic rank, candidates arranged in single-layer slots exhibit a higher harmonic winding factor that the one arranged in double-layers slots.

III. CASE STUDY

This study resumes the candidate treated in Part 1 [11]. It consists in a FSPMSM equipped with three phases in the armature arranged in eighteen double-layer slots and twelve poles in the rotor achieved by interior PMs. The slot-pole combination makes it possible the arrangement of each phase by connecting in parallel six coils.

A. BACK-EMF HARMONIC CONTENT

Following a start of slots-based investigation of the back-EMF harmonic content, three cases have been distinguished. These are characterized by three electrical shifts between adjacent back-EMF phasors, such that: $\alpha_{(2k+1)} = 2\pi, \frac{2\pi}{3}$, and $\frac{4\pi}{3}$. The corresponding star of slots and winding factors are regrouped in table 1.

B. TORQUE PRODUCTION CAPABILITY

This paragraph deals with both analytical and FEA predictions of the torque production capability of the FSPMSM under study. With its interior PMs, it belongs to the class of salient pole synchronous machines, developing an electromagnetic torque T_{em} which is the sum of a synchronizing component and a reluctant one [12], [13]. The design of the machine has been carried out in order to meet the following:

- a DC bus voltage $V_{DC} = 400$V leading to a maximum armature voltage $V_{max} \simeq 255$V.
- a maximum torque T_{max} of 180N.m achieved for an armature current of 188.25A,
- the corresponding base speed $\Omega_B = 2600$rpm,

Accounting for above specifications, the machine parameters have predicted. They are listed in table 2.

TABLE 1. Harmonic back-EMFs characterization.

Harmonic rank	Star of Slots	Electrical angle, Winding factor
18, 54, 90 ...		$\begin{cases} \alpha_e = 2\pi \\ k_w = 0 \end{cases}$
30, 66, 102 ...	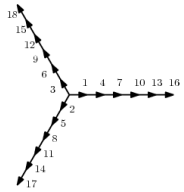	$\begin{cases} \alpha_e = \frac{4\pi}{3} \\ k_w = \|\cos(\frac{\pi}{6})\| \simeq 0.866 \end{cases}$
42, 78, 114 ...	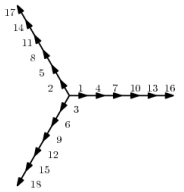	$\begin{cases} \alpha_e = \frac{2\pi}{3} \\ k_w = \|\cos(\frac{\pi}{6})\| \simeq 0.866 \end{cases}$

TABLE 2. Parameters of the FSPMSM under study.

Parameter	symbol	value
Pole pair number	p	6
no-load phase flux linkage	ϕ_{rms}	0.043Wb
direct inductance	L_d	480μH
quadrature inductance	L_q	689.56μH
armature resistance	r	57mΩ

With the armature current kept constant equal 188.25A, the variation of the electromagnetic torque T_{em} with respect to the torque angle ψ has been analytically-predicted and has led to the characteristic shown in Fig. 6. The same figure includes the results yielded by 2D FEA. One can notice a good agreement between the analytical and FEA results, with

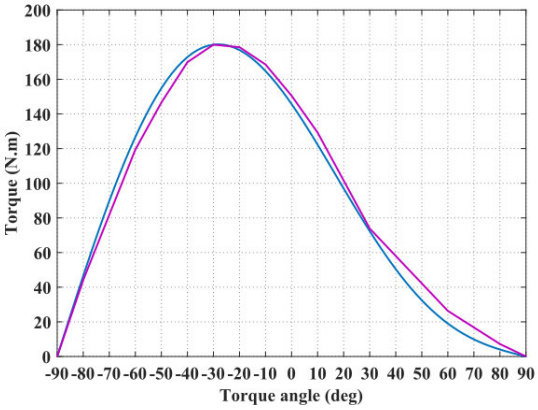

FIGURE 6. Electromagnetic torque T_{em} vs. the torque angle ψ. Legend: (blue): analytical results, (purple): FEA results.

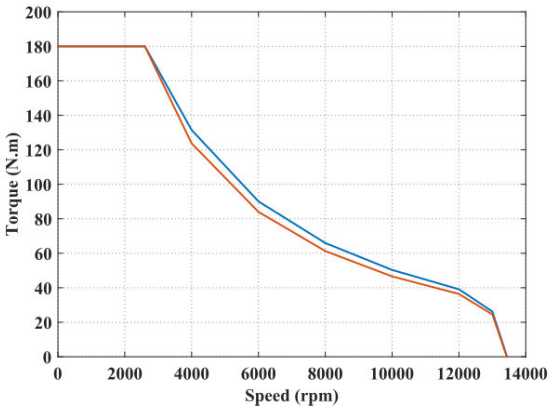

FIGURE 7. Torque-speed characteristic of the studied FSPMSM. Legend: (blue): analytical results, (orange): FEA results..

the maximum torque achieved for a torque angle, noted ψ_M, almost equal to $-\frac{\pi}{6}$.

In addition to the high torque requirements at low speeds, aerospace and automotive applications require a flux weakening operation over a wide speed range. For a given armature current, to achieve speeds over the base one, the torque angle ψ should be varied from Ψ_M to $-\frac{\pi}{2}$. The corresponding range of the speed Ω could be found out applying a numerical procedure such as the fixed point method.

The different steps of the developed fixed point-based numerical procedure dedicated to the prediction of the speed Ω are listed hereunder:

- for given values of the armature current I_{rms} and torque angle ψ,
- the speed Ω is increased starting from the base one $\Omega - B$, while the armature voltage V_{rms} is predicted using the phasor diagram characterizing the steady-state operation of salient pole synchronous machines with a reverse saliency [13], as follows:

$$V_{rms} = \sqrt{A(\Omega)^2 + B(\Omega)^2} \tag{8}$$

where:

$$\begin{cases} A(\Omega) = p\Omega\phi_{rms} + L_d p\Omega I_{rms}\sin(\psi) + rI_{rms}\cos(\psi) \\ B(\Omega) = L_q p\Omega I_{rms}\cos(\psi) + rI_{rms}\sin(\psi) \end{cases}$$

- V_{rms} is compared to V_{max}. If the difference is lower than a given error ϵ, then the corresponding speed would be the solution.

The maximum speed N_{max}, corresponding to the limit of the flux weakening range, is expressed as:

$$N_{max} = \frac{30}{\pi}\left(\frac{\sqrt{V_{max}^2 - (rI_{rms})^2}}{p(\phi_{rms} - L_d I_{rms})}\right) \simeq 13437.3rpm \tag{9}$$

The torque-speed characteristic has been analytically-predicted under a constant armature current of 188.25A. In the constant torque region, the torque angle has been kept constant $\psi = \psi_M$ leading to a base speed of 2600rpm. Then, for $V_{rms} = V_{max}$, the torque-speed characteristic in the flux weakening range has been predicted by reducing ψ from ψ_M to $-\frac{\pi}{2}$. The resulting characteristic is shown in Fig. 7.

The torque-speed characteristic has been also predicted by FEA. The obtained results are illustrated in Fig. 7. One can notice a good agreement between analytical and FEA results.

C. LOSS AND EFFICIENCY ASSESSMENT

Taking into account the fact that the iron loss and particularly the PM eddy current ones could be critical in FSPMSMs, a special attention is paid to their prediction hereunder.

1) IRON LOSS PREDICTION

This paragraph deals with a FEA-based prediction of the iron loss of the studied FSPMSM. The eddy current, hysteresis, and excess loss have been predicted considering two on-load operating points, as:

- constant torque region: for a speed of 2000rpm corresponding to a fundamental frequency of the armature current of 200Hz,
- flux weakening region: for a speed of 4000rpm corresponding to a fundamental frequency of the armature current of 400Hz.

The stator and rotor cores are made of M270-35A lamination that has a stacking coefficient of 0.95, a thickness of 0.35mm, a mass density of 7650kg.m^{-3}, and a conductivity of 1923100Ω.m.

a: IRON LOSS PREDICTION IN THE CONSTANT TORQUE REGION

The iron loss characteristic $P_{iron}(B)$ of the used laminated material M270-35A, for a frequency of 200Hz, is shown in Fig. 12. Based on this latter, the eddy current, hysteresis, and excess loss coefficients, of the *Steinmetz* model have been identified as: $C_{ec} = 0.3875$, $C_{hyst} = 148.9212$, and $C_{ex} = 1.4824$, respectively. These have been implemented in the developed FEA model.

Figs. 9, 10, and 11 illustrate the variations of the eddy current, hysteresis, and excess loss over time, respectively.

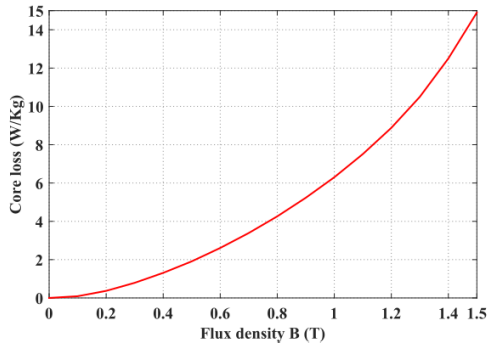

FIGURE 8. Iron loss characteristic $P_{iron}(B)$ of the M270-35A for a frequency of 200Hz.

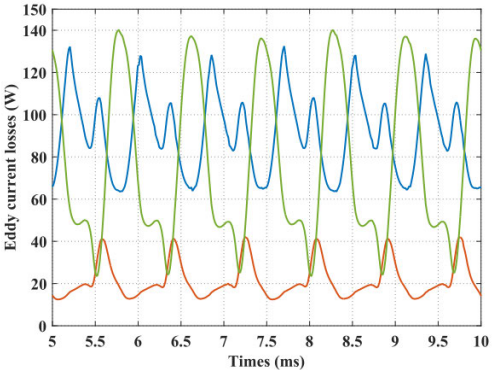

FIGURE 9. Eddy current loss versus time for a speed of 2000rpm. Legend: (orange): rotor core loss, (blue): stator core loss, (green): PM eddy current loss.

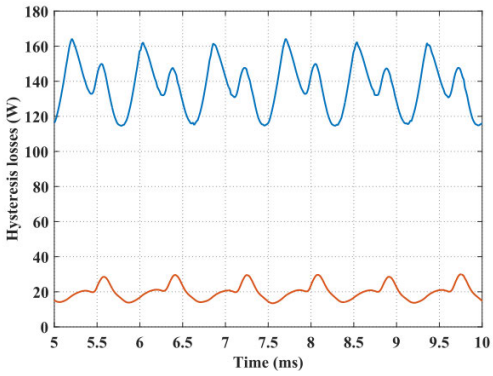

FIGURE 10. Hysteresis loss versus time for a speed of 2000rpm. Legend: (orange): rotor core loss, (blue): stator core loss.

Table 3 gives a summary of the mean values of the iron loss components predicted for a speed of 2000rpm. It is to be noted that the rotor iron loss are far from being negligible and that they are weighted by their PM eddy current component.

2) IRON LOSS PREDICTION IN THE CONSTANT POWER REGION

The iron loss characteristic $P_{iron}(B)$ of the used laminated material M270-35A for a frequency of 400Hz is provided

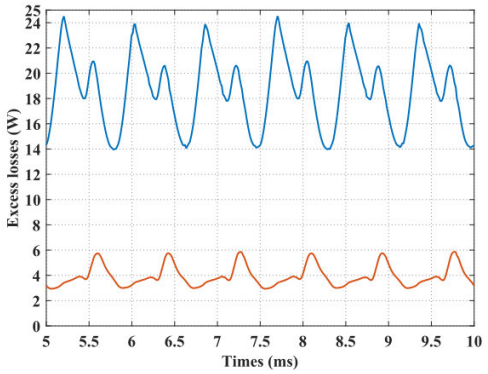

FIGURE 11. Excess loss versus time for a speed of 2000rpm. Legend: (orange): rotor core loss, (blue): stator core loss.

TABLE 3. Mean values of the different components of the iron loss for a speed of 2000rpm.

Loss (W)	Eddy current	Hysteresis	Excess	Total
Stator core	90.75	136.22	18.62	245.59
Rotor core	21.15	20.17	3.9	45.22
PMs	76.94	–	–	76.94
			Iron loss	367.75

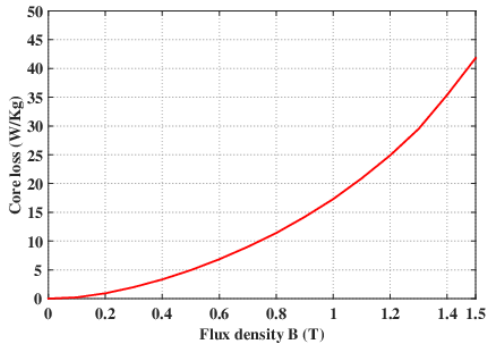

FIGURE 12. Iron loss characteristic $P_{iron}(B)$ of the M270-35A for a frequency of 200Hz.

in Fig. 12, based on which the coefficients of the *Steinmetz* model have been identified as: $C_{ec} = 0.3875$, $C_{hyst} = 187.5593$, and $C_{ex} \simeq 0$, respectively.

Figs. 13 and 14 illustrate the variation of the eddy current and hysteresis loss over time, for a speed of 4000rpm.

Table 4 summarises the means values of the different iron loss components, predicted for a speed of 4000rpm. It is to be noted that the iron loss are lower in the stator magnetic circuit than in the rotor one, where the PM eddy current loss represent the major part (71.6% of the rotor iron loss).

3) EFFICIENCY MAPS

A combined FEA-analytical procedure has been developed in order to predict the drive efficiency. As previously treated, the iron loss have been computed by FEA. While, the Joule, mechanical, and inverter loss have been analytically-predicted.

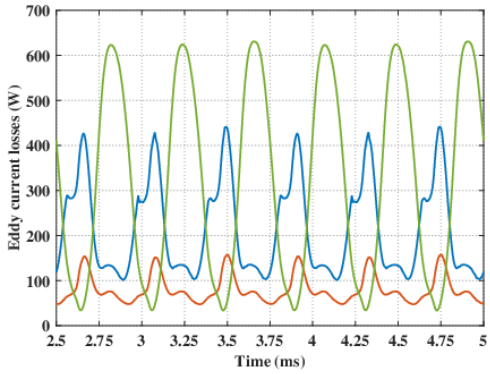

FIGURE 13. Eddy current loss versus time for a speed of 4000rpm. Legend: (orange): loss in the rotor core, (blue): loss in the stator core, (green): loss in the PMs.

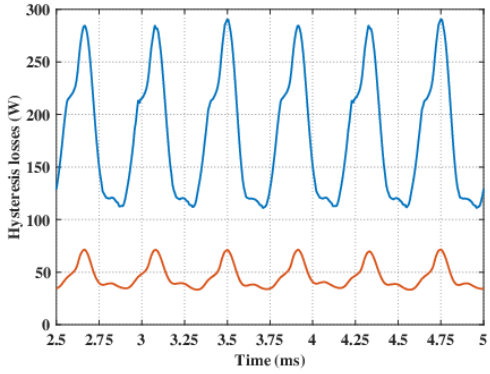

FIGURE 14. Hysteresis loss versus time for a speed of 4000rpm. Legend: (orange): rotor core loss, (blue): stator core loss.

TABLE 4. Mean values of the different components of the iron loss of the prototyped FSPMSM for a speed of 4000rpm.

Loss (W)	Eddy current	Hysteresis	Total
Stator core	215.27	172.52	387.79
Rotor core	81.55	47.57	129.12
PMs	326.32	–	326.32
		Total	843.23

Two efficiency maps of the FSPMSM under study (motor EM1) have been considered, such that:

- Fig. 15(a) gives the efficiency map under constant torque operation (increasing the armature voltage, the torque angle kept constant),
- Fig. 15(b) gives the efficiency map under constant power operation (decreasing the torque angle, the armature voltage kept constant at its maximum value).

As expected, high efficiencies are achieved under constant torque operation. While under constant power one, a part of the armature current is used for the flux weakening, along with an increase of the machine iron and friction loss and the inverter commutation ones.

D. EXPERIMENTAL VALIDATION

1) STUDY STATEMENT

The Institute of Vehicle Concepts of the German Aerospace Center (DLR) has been working on the development of future

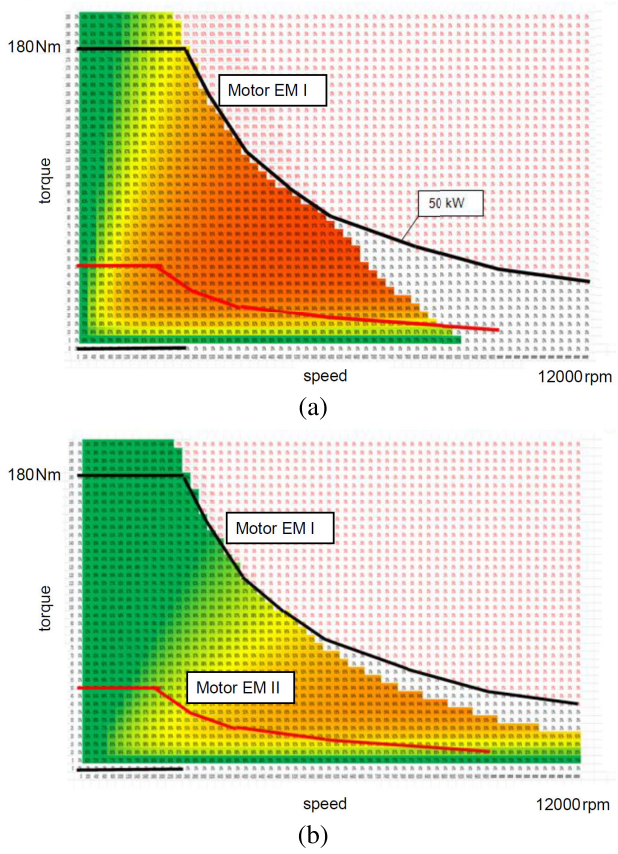

FIGURE 15. Drive efficiency η maps. Legend 1: (a) constant torque operation, (b) constant power operation. Legend 2: (red) $\eta \geq 90\%$, (yellow) $80\% \leq \eta < 90\%$, (green) $\eta < 80\%$.

FIGURE 16. Prototype of the NGC-UMV concept.

vehicle concepts for road and rail within different transport research programs. The aim is to design efficient, sustainable and affordable mobility concepts, allied to new energy sources as well as to automation and digital traffic guidance network systems.

Within the DLR internal project Next Generation Car (NGC), the Institute of Vehicle Concepts is currently developing an Urban Modular Vehicle (UMV) that makes it possible the assessment and test of novel urban and aerospace technologies. Of particular interest is the NGC-UMV concept, shown in Fig. 16. Thanks to its modular design, the

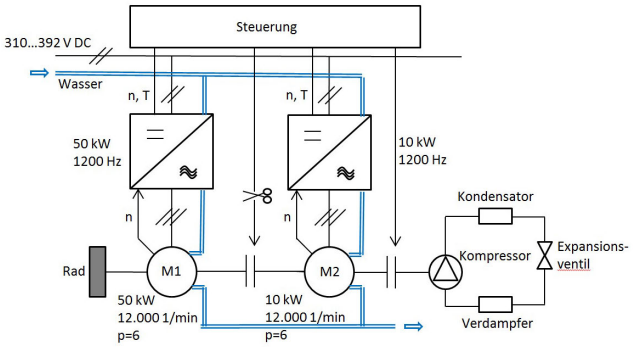

FIGURE 17. Scheme of the two-in-one-motor system.

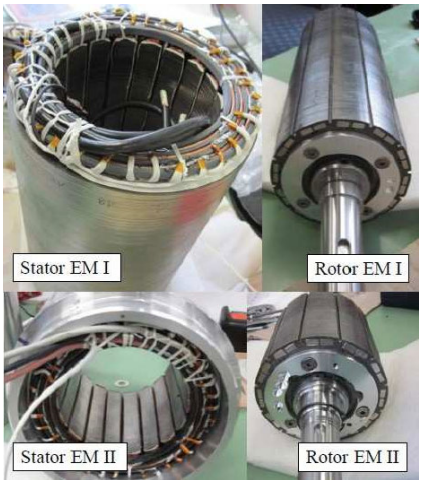

FIGURE 18. Photos of the stators and rotors of EM1 and EM2.

NGC-UMV concept could be equipped with different drive train topologies, among which the so-called ''two-in-one motor system'' which is currently under development. It consists in a dual motor concept, made up of:

- EM1: a FSPMSM with a rated power of 50kW acting as propeller,
- EM2: a FSPMSM with a rated power of 10kW driving the air conditioning compressor when required and boosting the propulsion when possible.

as illustrated in the scheme of Fig. 17.

Photos of the stators and rotors of the prototyped EM1 and EM2 are shown in Fig. 18. EM1 and EM2 are mechanically-coupled by the electromagnetic clutch illustrated in Fig. 19. Both FSPMSMs may be separately-operated using independent inverters. A photo of the inverter feeding EM1 is given in Fig. 20. It is equipped with SiC power switches, and designed for water cooling. It has a rated power of 60kVA.

The motivation behind the development of a dual motor concept comes from a trend to design a single drive including most of the energy converters of electric cars, in an attempt to emulate the operation of their internal combustion engine (ICE)-propelled counterparts. Indeed, ICE powertrains have

FIGURE 19. Electromagnetic clutch coupling EM1 and EM2.

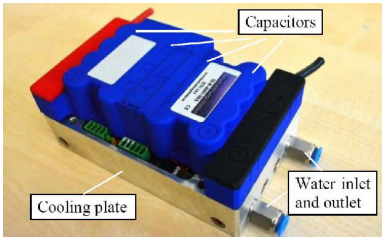

FIGURE 20. Photo of the inverter feeding EM1.

been designed in such a way that most of the auxiliary units like starter, generator, air conditioning compressor, water pump, are driven by the ICE shaft through pulley-belt systems. Integrating different electric machines in one electro-mechanical set has emerged with the necessity to improve the compactness of hybrid propulsion systems.

Within this frame work, *Ben Hamadou et al.* proposed in [17] a single-stator dual-rotor PM machine intended to hybrid heavy vehicles. It consists in two concentric PM machines with a stator sandwiched between an inner rotor and an outer one. In [18], *Sun et al.* treated the analysis and control of a complementary magnetic-geared dual-rotor motor. This concept has demonstrated its effectiveness as an electrical power split device for series-parallel hybrid powertrains. The same application has been considered in [19] where a dual-rotor magnetically-geared power device has been proposed. In [20], *Dalal* and *Kumar* proposed an electromagnetic concept equipped with a PM rotor and a cage one dedicated to automotive applications. In [21], *Li et al.* treated the design and optimization of a dual-rotor machine for traction applications. It has surface-mounted PMs in the outer rotor and a synchronous reluctance in the inner one.

Beyond automotive applications, dual motor concepts have been found viable in several other applications. In [22], *Wu et al.* developed an approach to design of a pulsed alternator which is based on a dual rotor PM concept dedicated to military applications. Both inner and outer rotors are equipped with a *Halbach* PM array. In [23], *Golovanov et al.* investigated the power density of different electrical machine topologies intended for transport applications with emphasis on the aerospace one. They have found that the dual-rotor topology exhibits the best power to mass ratio.

2) TORQUE-SPEED CHARACTERISTIC

A vector control strategy has been implemented in the motor EM1 drive. A scope of the phase current for a torque of 4N.m

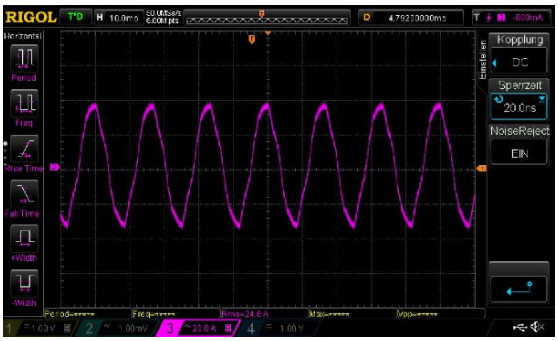

FIGURE 21. Phase current for a torque of 4N.m and a speed of 600rpm.

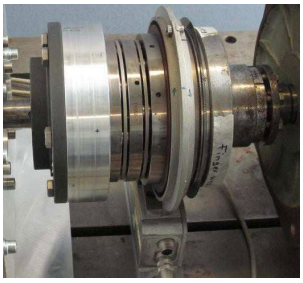

FIGURE 22. Torque and speed sensors mounted in between the two-in-one-motor system and the load machine.

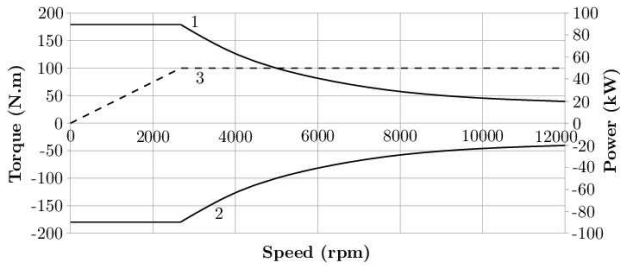

FIGURE 23. Torque-speed characteristic during acceleration, (2) torque-speed characteristic under regenerative braking, (3) power-speed characteristic, measured for a current of 188.25A.

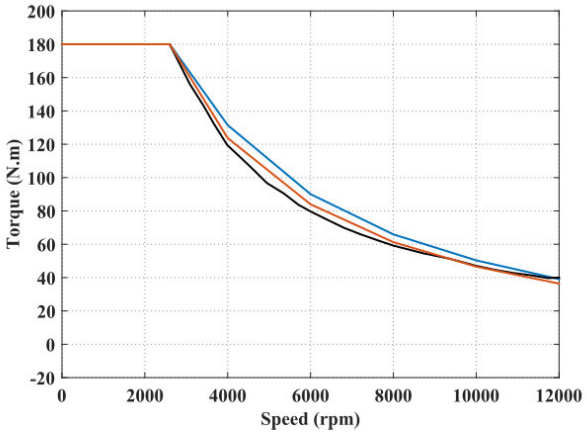

FIGURE 24. Torque-speed characteristic of the prototyped FSPMSM. Legend: (black) experimental data, (orange) FEA results, (blue) analytical results.

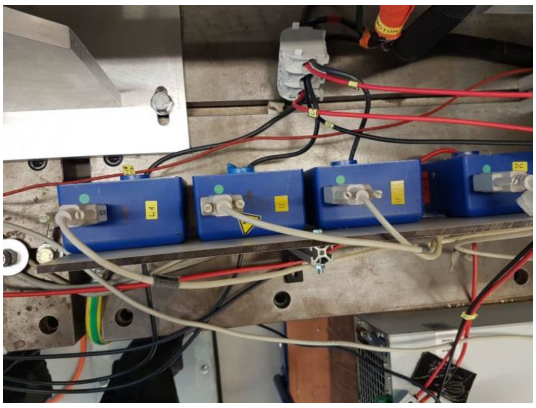

FIGURE 25. Current sensors to be interfaced to the wattmeter used for the measurement of the electric power absorbed by motor M1.

and a rotor speed of 600rpm is ilustrated in Fig. 21. The measured waveform has a relatively lower harmonic distortion than the back-EMF one because, even with the parallel connection of the phase coils, the inductive behavior of the FSPMSM circuits remains dominant. The torque and speed are measured using dedicated sensors which are mounted between the two-in-one-motor and the load machine. A photo of both sensors is given in Fig. 25.

The torque-speed characteristic has been experimentally-accessed, considering a constant armature current equal to 188.25A. The torque angle has been initially kept constant equal to $-\frac{\pi}{6}$, and the speed has been increased until reaching 2600rpm, corresponding to the maximum armature voltage. Then, the flux weakening operation has been practically-implemented by keeping the armature voltage at its maximum value and increasing its frequency while reducing the torque angle. Due to mechanical constrains, the speed has been limited to 12000rpm. The resulting torque-speed characteristic is shown in the top of Fig. 23. Furthermore, a special attention has been also paid to the generator operation which corresponds, in the case of propulsion applications, to the regenerative braking. The corresponding torque-speed characteristic is illustrated in the bottom of Fig. 23. For the sake of comparison, Fig. 24 brings together the characteristics given in Figs. 7 and 23. A quite acceptable match between FEA and experimental results has been found.

3) POWER FLOW ANALYSIS

a: NO-LOAD TEST: LOSS

The sum of the iron and mechanical loss have been measured at no-load according to the EN 60034-2-1 standard. For that, current sensors have been linked to the armature phases as shown in Fig. 25. These have been interfaced to the wattmeter given in Fig. 26 to measure the electric power absorbed by motor M1 at no-load operation. This latter is characterized by low values of the armature current so that the copper loss P_c

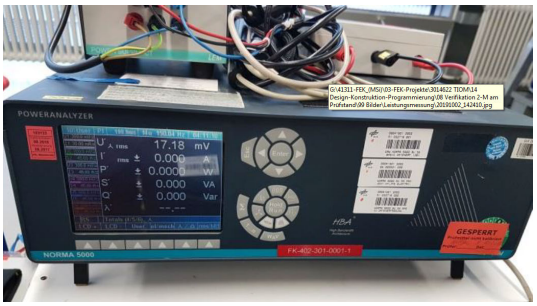

FIGURE 26. Wattmeter used for the measurement of the electric power absorbed by motor M1.

TABLE 5. Electric power P_0 (W) absorbed by the armature of M1 at no-load operation, the predicted mechanical loss P_m (W), and extracted iron loss P_i (W), versus the rotor speed N (rpm).

N	P_0	P_m	P_i	N	P_0	P_m	P_i
400	78	2.52	75.48	3000	630	34.51	595.49
600	110	4.02	105.98	3200	659	38.09	620.91
800	141	5.68	135.32	3400	712	41.83	670.17
1000	181	7.5	173.5	3600	746	45.73	700.27
1200	226	9.48	216.52	3800	785	49.79	735.21
1400	269	11.62	257.38	4000	844	54.01	790.99
1600	312	13.92	298.08	4200	889	58.39	830.61
1800	352	16.38	335.62	4400	933	62.93	870.07
2000	394	19	375	4600	978	67.63	910.34
2200	432	21.78	410.22	4800	1023	72.49	950.51
2400	470	24.72	445.28	5000	1078	77.51	1000.49
2600	528	27.82	500.18	5200	1113	82.69	1030.31
2800	582	31.09	550.91	5400	1159	88.03	1070.97

could be neglected. The measurements of the no-load power P_0 are provided in table 5.

Accounting for the difficulties to extract the mechanical loss P_m from P_0, they have been predicted using the data sheet of the bearings equipping motor M1. The bearing loss can be approximated by a constant frictional torque. This latter has been predicted using [24] which has led to the variation of the mechanical loss due to the bearing friction P_b versus the rotor speed N (rpm) as:

$$P_b = 5502.10^{-6}N \tag{10}$$

Moreover, due to the grooves in the surface of the rotor, the latter generates ventilation loss P_v. These increase quadratically with the speed as follows:

$$P_v = 2.10^{-6}N^2 \tag{11}$$

Finally, the mechanical loss P_m are expressed in terms of the speed as follows:

$$P_m = 5502.10^{-6}N + 2.10^{-6}N^2 \tag{12}$$

The iron loss P_i are extracted from the no-load loss as:

$$P_i = P_0 - P_m \tag{13}$$

Table 5 provides de mechanical and iron loss for the speeds considered in the no-load test. Table 6 recalls the FEA results given in paragraph III-C1 and compare them to the iron loss extracted from the no-load test. The shift between the

TABLE 6. Comparison between the iron loss predicted in paragraph III-C1 and those extracted from the no-load test.

	Iron loss P_i (W)	
Speed (rpm)	FEA	experimental
2000	367.75	375
4000	843.23	790.99

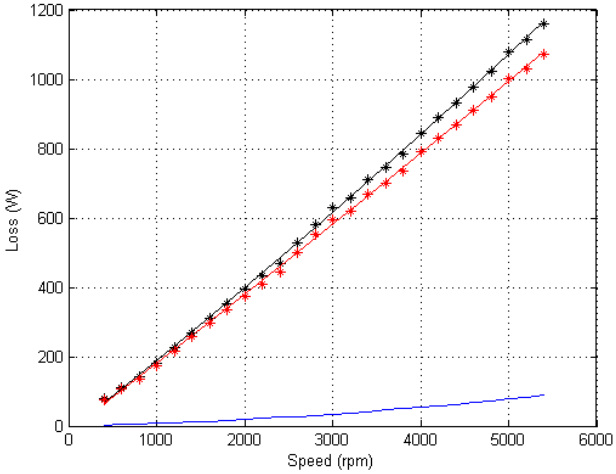

FIGURE 27. Loss at no-load operation. Legend: (black stars) measured no-load loss, (black line) extrapolation of the measured no-load loss, (blue) predicted mechanical loss, (red stars) iron loss extracted from the measured no-load loss, (red line) extrapolation of the iron loss.

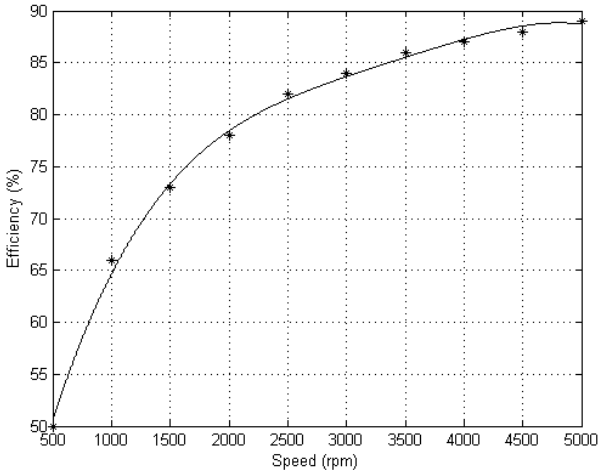

FIGURE 28. Measured efficiency vs. the speed for a constant torque of 50Nm.

FEA and experimental results is mainly due to fact that the experimental test has been carried out at no-load operation with a negligible armature magnetic reaction.

Fig. 27 shows P_0, P_m, and P_i versus the speed N.

b: ON-LOAD TEST: EFFICIENCY AND POWER DENSITY

An on-load test has been carried out at a constant load torque of 50Nm and for a linear variation of the speed. Following the measurement of the power absorbed by the armature P_a and the output power available in the shaft P_s using the torque

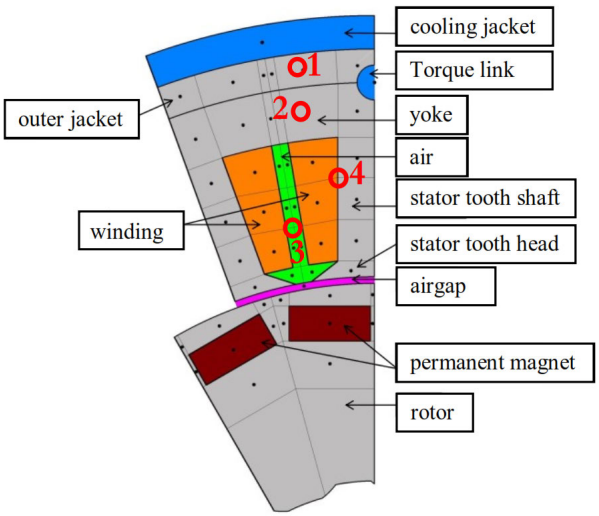

FIGURE 29. Thermal replacement model including the locations of the temperature sensors 1, 2, 3, and 4 (in red color).

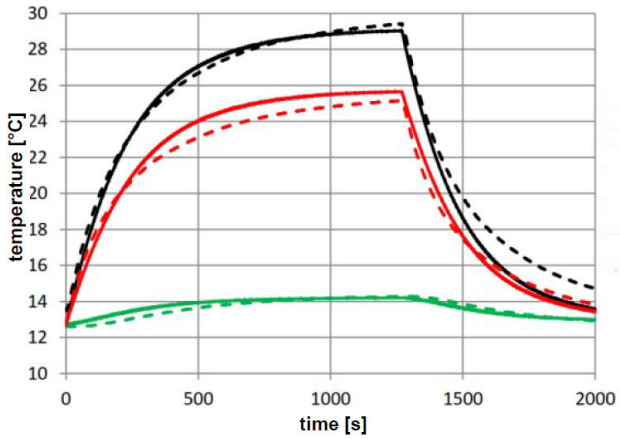

FIGURE 30. Temperature profiles in selected stator locations, following a load pulse. Legend 1: (dashed line) thermal model results, (continuous line) test results. Legend 2: (green) sensor 2, (red) sensor 4, (black) sensor 3.

and speed sensors, the efficiency η has been determined as follows:

$$\eta = \frac{P_s}{P_a} \tag{14}$$

The obtained results are shown in Fig. 28. One can notice that the efficiency remains lower than 90% which is due the high pole edge leakage flux of the prototyped machine [11].

Let us call L_t and D_o, the total axial length and the outer diameter of M1 with $L_t = 0.3$m and $D_o = 0.2$m, one can predict the power density as follows:

$$\xi = \frac{P_s}{\frac{\pi}{4} D_o^2 L_t} \tag{15}$$

which gives for the considered load torque and speed range:

$$\xi(W/m^3) = 555N(rpm) \tag{16}$$

4) THERMAL BEHAVIOUR ASSESSMENT

Accounting for the FEA-analytical procedure considered in paragraph III-C3, a thermal replacement model, based on the approaches developed in [25], [26], has been established. It has been numerically-implemented considering the study domain illustrated in Fig. 29.

For the sake of validation of the established thermal model, four temperature sensors have been appropriately-installed in the stator as shown in Fig. 29. With the temperature of the water in the cooling jacket kept constant equal to 13°C (sensor 1), a load step characterized by an armature current of 50A, applied during 22min, has led to the evolution with respect to time of the temperatures, measured by sensors 2, 3, and 4, illustrated in Fig. 30. The same figure shows the temperatures analytically-predicted using the established thermal model. One can notice a quite acceptable agreement between the analytical and experimental results.

IV. CONCLUSION

This work was devoted to a class of FSPMSMs equipped with phases made up of one coil parallel branches. These are reputed by their enhanced open-circuit fault-tolerance capability. The second part of the work was aimed at an investigation of the possible circulation of harmonic currents in the loops created by the parallel connections of the coils. This has been carried out considering a systematic application of the star of slots approach to investigate the harmonic content of the back-EMFs. It has been found that all identified candidates exhibit the potential to reject the circulating harmonic currents.

A case study has been treated considering a 3 phase, 18 double-layer slot, 12 pole FSPMSM. The slot-pole combination enabled the arrangement of the three phases in six parallel branches including a single coil each. A special attention has been paid to the torque production capability with emphasis on the torque-speed characteristic. The latter has been analytically-predicted and validated by FEA.

Moreover, a power flow analysis, with emphasis on the iron loss, has been carried out. It enabled the drawing of the drive efficiency maps considering, separately, the constant torque and flux weakening operations. The case study has been achieved by an experimental validation of the torque-speed characteristic and of a dedicated thermal model.

In light of this work, it has to be underlined that, in spite of their intrinsic potential to discard circulating harmonic currents, not all identified FSPMSMs could be regarded as viable candidates for applications requiring a high open-circuit fault tolerance. This latter is compromised by a low fundamental winding factor in some identified candidates which affect their torque production capability. Moreover, even with a high fundamental winding factor, a special attention should be paid to the selection of the slot-pole combinations in order to achieve a low cogging torque and reduced radial forces that cause noise and vibration. This said, and for viable candidates such as the case study one, there is some way to go before

reaching a mature technology. Beyond the design improvement, an enhancement of the fault tolerance capability could be gained through the synthesis of dedicated torque recovery control strategies under open-circuit faulty scenarios. This represents one of the major outlooks of the present work.

REFERENCES

[1] L. P. Di Noia and R. Rizzo, "Design of a five-phase permanent-magnet motor for the electric steering of an aircraft nose landing gear," *IET Electr. Syst. Transp.*, vol. 7, no. 4, pp. 327–333, Dec. 2017.
[2] Q. Shen, C. Yue, C. H. Goh, and D. Wang, "Active fault-tolerant control system design for spacecraft attitude maneuvers with actuator saturation and faults," *IEEE Trans. Ind. Electron.*, vol. 66, no. 5, pp. 3763–3772, May 2019.
[3] Y. Shang, X. Li, H. Qian, S. Wu, Q. Pan, L. Huang, and Z. Jiao, "A novel electro hydrostatic actuator system with energy recovery module for more electric aircraft," *IEEE Trans. Ind. Electron.*, vol. 67, no. 4, pp. 2991–2999, Apr. 2020.
[4] L. Zhang, Y. Fan, R. D. Lorenz, R. Cui, C. Li, and M. Cheng, "Design and analysis of a new five-phase brushless hybrid-excitation fault-tolerant motor for electric vehicles," *IEEE Trans. Ind. Appl.*, vol. 53, no. 4, pp. 3428–3437, Jul. 2017.
[5] S. Cash, Q. Zhou, O. Olatunbosun, H. Xu, S. Davis, and R. Shaw, "New traction motor sizing strategy for an HEV/EV based on an overcurrent-tolerant prediction model," *IET Intell. Transp. Syst.*, vol. 13, no. 1, pp. 168–174, Jan. 2019.
[6] X. Zhao, S. Niu, X. Zhang, and W. Fu, "Design of a new relieving-DC-saturation hybrid reluctance machine for fault-tolerant in-wheel direct drive," *IEEE Trans. Ind. Electron.*, vol. 67, no. 11, pp. 9571–9581, Nov. 2020.
[7] I. Boldea, L. Tutelea, and C. I. Pitic, "PM-assisted reluctance synchronous motor/generator (PM-RSM) for mild hybrid vehicles: Electromagnetic design," *IEEE Trans. Ind. Appl.*, vol. 40, no. 2, pp. 492–498, Mar. 2004.
[8] A. Fatemi, T. W. Nehl, X. Yang, L. Hao, S. Gopalakrishnan, A. M. Omekanda, and C. S. Namuduri, "Design optimization of an electric machine for a 48-V hybrid vehicle with comparison of rotor technologies and pole-slot combinations," *IEEE Trans. Ind. Appl.*, vol. 56, no. 5, pp. 4609–4622, Sep. 2020.
[9] M. S. Trivedi and R. K. Keshri, "Evaluation of predictive current control techniques for PM BLDC motor in stationary plane," *IEEE Access*, vol. 8, pp. 46217–46228, 2020.
[10] I. Abdennadher and A. Masmoudi, "Armature design of low-voltage FSPMSMs: An attempt to enhance the open-circuit fault tolerance capabilities," *IEEE Trans. Ind. Appl.*, vol. 51, no. 6, pp. 4392–4403, Nov. 2015.
[11] A. Masmoudi, S. Mkaouar, A. Maaoui, and M. Schier, "Fractional-slot PMSMs with one coil parallel branches made phases—Part I: Investigation study," *IEEE Access*, vol. 9, pp. 131322–131335, 2021.
[12] T. A. Lipo, *Introduction to AC Machine Design*. Hoboken, NJ, USA: Wiley, 2017.
[13] A. Masmoudi, *Control Oriented Modelling of AC Electric Machines*. Singapore: Springer, 2018.
[14] Z. Q. Zhu, D. Howe, E. Bolte, and B. Ackermann, "Instantaneous magnetic field distribution in brushless permanent magnet DC motors—Part I: Open-circuit field," *IEEE Trans. Magn.*, vol. 29, no. 1, pp. 124–135, Jan. 1993.
[15] L. Alberti and N. Bianchi, "Theory and design of fractional-slot multilayer windings," *IEEE Trans. Ind. Appl.*, vol. 49, no. 2, pp. 841–849, Mar. 2013.
[16] I. Abdennadher and A. Masmoudi, "Star of slots-based graphical assessment of the back-EMF of fractional-slot PM synchronous machines," in *Proc. 10th Int. Multi-Conf. Syst., Signals Devices (SSD)*, Hammamet, Tunisia, Mar. 2013, pp. 1–8.
[17] G. B. Hamadou, A. Masmoudi, I. Abdennadher, and A. Masmoudi, "Design of a single-stator dual-rotor permanent-magnet machine," *IEEE Trans. Magn.*, vol. 45, no. 1, pp. 127–132, Jan. 2009.
[18] L. Sun, M. Cheng, J. Zhang, and L. Song, "Analysis and control of complementary magnetic-geared dual-rotor motor," *IEEE Trans. Ind. Electron.*, vol. 63, no. 11, pp. 6715–6725, Nov. 2016.
[19] P. Chmelicek, S. D. Calverley, R. S. Dragan, and K. Atallah, "Dual rotor magnetically geared power split device for hybrid electric vehicles," *IEEE Trans. Ind. Appl.*, vol. 55, no. 2, pp. 1484–1494, Mar. 2019.
[20] A. Dalal and P. Kumar, "Design, prototyping, and testing of a dual-rotor motor for electric vehicle application," *IEEE Trans. Ind. Electron.*, vol. 65, no. 9, pp. 7185–7192, Sep. 2018.
[21] Y. Li, D. Bobba, and B. Sarlioglu, "Design and optimization of a novel dual-rotor hybrid PM machine for traction application," *IEEE Trans. Ind. Electron.*, vol. 65, no. 2, pp. 1762–1771, Feb. 2018.
[22] S. Wu, W. Zhao, S. Wu, and S. Cui, "Design and analysis of counter-rotating dual rotors permanent magnet compensated pulsed alternator," *IEEE Trans. Plasma Sci.*, vol. 45, no. 7, pp. 1101–1107, Jul. 2017.
[23] D. Golovanov, L. Papini, D. Gerada, Z. Xu, and C. Gerada, "Multidomain optimization of high-power-density PM electrical machines for system architecture selection," *IEEE Trans. Ind. Electron.*, vol. 65, no. 7, pp. 5302–5312, Jul. 2018.
[24] SKF. *Bearing Caluculator*. Accessed: 2020. [Online]. Available: https://www.skf.com/de/products/bearings-units-housings/operatingtemperature-and-speed/friction-powerloss-startingtorque/index.html
[25] I. Bouzidi, A. Masmoudi, and N. Bianchi, "Electromagnetic/thermal design procedure of an aerospace electric propeller," *IEEE Trans. Ind. Appl.*, vol. 51, no. 6, pp. 4364–4371, Nov. 2015.
[26] Z. Kuang, S. Wu, B. Du, H. Xu, S. Cui, and C. C. Chan, "Thermal analysis of fifteen-phase permanent magnet synchronous motor under different fault tolerant operations," *IEEE Access*, vol. 7, pp. 81466–81480, 2019.

AHMED MASMOUDI (Senior Member, IEEE) received the B.S. degree from the Sfax Engineering National School (SENS), University of Sfax, Sfax, Tunisia, in 1984, the Ph.D. degree from Pierre and Marie Curie University, Paris, France, in 1994, and the Postdoctoral Research Habilitation degree from SENS, in 2001, all in electrical engineering.

In 1988, he joined Tunisian University, where he held different positions involved in both education and research activities. He is currently a Full Professor in electric power engineering with SENS. He is also the Head of the Research Laboratory on renewable energies and electric vehicles, and the Coordinator of the master on sustainable mobility actuators: research and technology. He is the author of more than 100 papers, 24 among which are published in IEEE Transactions. He is the author and coauthor of four books and is the Co-Inventor of a U.S.-patent. He has presented up to 11 keynote speeches in international conferences. He has been the Chair of the Program and Publication Committees of the International Conference on Ecological Vehicles and Renewable Energie (EVER), annually-organized in Monaco, since 2007. He is the Head of the Founding Committee of the International Conference on Sustainable Mobility Applications, Renewables, and Technology (SMART) that has been organized in the Australian College of Kuwait, in 2015. His research interests include the design of new topologies of AC machines and the implementation of advanced and efficient control strategies in drives and generators, applied to automotive, and to renewable energy systems.

SAHAR MKAOUAR received the B.S. degree in electromechanical engineering from the Sfax Engineering National School (SENS), University of Sfax, Sfax, Tunisia, in 2019, and the M.Sc. degree in sustainable mobility actuators: research and technology (SMART) from SENS, in 2021.

She has pursued the second year of her master's program and defended her thesis at Kassel University, Kassel, Germany, within the Erasmus Exchange Program 20210607-ENIS-KA107. Her current interest include design, sizing, and optimization of permanent magnet machines dedicated to automotive, and aerospace applications.

AICHA MAAOUI received the B.S. degree in electromechanical engineering from the Sfax Engineering National School (SENS), University of Sfax, Sfax, Tunisia, in 2019, and the master's degree in sustainable mobility actuators: research and technology (SMART) from SENS, in 2020. She developed her master project with the German Aerospace Center (DLR), Stuttgart, Germany. She is currently pursuing the Ph.D. degree in the design of permanent magnet motors applied to electric propulsion systems.

MICHAEL SCHIER (Member, IEEE) received the Diploma and Ph.D. degrees in electrical engineering with specialization in energy technologies and electrical drives with the Technical University of Kaiserslautern, Germany.

From 1995 to 1999, he was involved in the development of electrical machines and power electronics for starter-alternators with the Department Electric Vehicles, Siemens Company, Würzburg, Germany. From 1999 to 2005, he was responsible for the development of blowers with electrical commutated motors and for automotive applications at Ebmpapst Company. Before his work at DLR, he was the Leader of Power Electronics Development at Catem-Develec, a Daughter Company of Eberspächer Company. Since 2007, he has been working in the research area with the German Aerospace Center, Stuttgart, Germany, where he first was responsible for the development of alternative drives within the Institute of Vehicle Concepts. He is currently the Head of the Department of Vehicle Energy Concepts. The main topics of his scientific work were combined permanent magnet-electrically stator excited synchronous machines, starter-alternators for automotive application, electronically-commutated motors for axial and radial blowers, high speed electric turbo-chargers, high torque machines for in-wheel motors for aircraft autonomous taxiing and double motor systems with corresponding publications on international conferences.